Eur. Phys. J. B **18**, 31–38 (2000)

THE EUROPEAN PHYSICAL JOURNAL B

EDP Sciences
© Società Italiana di Fisica
Springer-Verlag 2000

The origin of the redshift in Brillouin spectra of silica films containing tin nanoparticles

A. Li Bassi[1,2], C.E. Bottani[1,a], B.K. Tanner[2], A. Stella[3], P. Tognini[3], P. Cheyssac[4], and R. Kofman[4]

[1] INFM-Dipartimento di Ingegneria Nucleare, Politecnico di Milano, Via Ponzio 34/3, 20133 Milano, Italy
[2] Department of Physics, University of Durham, South Road, Durham DH1 3LE, UK
[3] INFM-Dipartimento di Fisica "A. Volta", Università degli Studi di Pavia, Via A. Bassi 6, 27100 Pavia, Italy
[4] Laboratoire de Physique de la Matière Condensée, URA 190, Université de Nice-Sophia Antipolis, 06108 Nice Cedex, France

Received 30 March 2000 and Received in final form 24 July 2000

Abstract. The abrupt change of velocity in surface acoustic waves in thin films of amorphous SiO_x containing nanometre scale β-Sn crystals is shown to be directly associated with the size-dependent melting of the nanoparticles, confirming preliminary experiments. High resolution thin film powder diffraction using synchrotron radiation shows that the abrupt redshift in the Brillouin spectra satellites occurs at the same temperature as the melting of the nanoparticles, evident for the loss of the Bragg peaks. Effective medium theory is used to explain the origin of the anomaly. A central peak in the Brillouin spectrum, the intensity of which shows a maximum at the melting temperature, can be interpreted in terms of overdamped fluctuations in the dielectric function. The melting temperature as a function of particle size is in agreement with theoretical predictions. No evidence for strain could be found on the X-ray diffraction profiles; the a- and c-axis thermal expansion coefficients are the same as those in bulk tin.

PACS. 61.46.+w Clusters, nanoparticles, and nanocrystalline materials – 78.35.+c Brillouin and Rayleigh scattering; other light scattering – 64.70.Dv Solid-liquid transitions – 43.35.+d Ultrasonics, quantum acoustics, and physical effects of sound

1 Introduction

Aggregates of atoms in the nanometer size range (currently called nanoparticles) exhibit properties which can be considered intermediate in several respects between those characterizing simple molecules on the one side and bulk materials on the other side. Recently they have been the object of theoretical and experimental work, both in the case of semiconductor quantum dots and metal nanocrystals [1–4]. The main motivation for the growing interest in these systems is related to the possibility of tailoring, to a considerable extent, their physical behaviour on the basis of size.

Here we shall confine our attention to metal nanoparticles. It has been established [4] that when the radius R becomes smaller than 1 nm, relevant quantum effects show up, when discrete effects are observed in the distribution of the electron energy levels. Above that size, the width of the discrete levels becomes comparable or larger than the separation between them, so that we enter a regime where the conduction band is quasi continuous and the behaviour of the nanoparticles progressively approaches that of the bulk metal, when the radius becomes approximately 20 nm [4]. In the intermediate size range 1 nm $< R <$ 20 nm, significant deviations with respect to the bulk properties can be detected and studied, concerning *e.g.* thermodynamic properties (melting temperature and latent heat of fusion [3]), optical properties (energy position and width of surface plasma resonances [5]), ultrafast electron dynamics, as long as the size is smaller than the electron mean free path [6].

In particular, when the ratio of the number of surface atoms to the total number of atoms becomes non negligible the melting temperature of the particles decreases down to about 2/3 T_0 [7], since the reduced number of bonds on the surface causes an enhancement of thermal vibration.

The melting temperature T_{M} of a particle of radius R was calculated by Semenchenko [8,9] from a classical point of view. For $R > 15$ nm he predicted

$$T_{\mathrm{M}} = T_0 \exp\left(-\frac{2\gamma_{\mathrm{sl}}}{\rho L R}\right) \tag{1}$$

where T_0 is the bulk melting temperature, ρ the volume mass density, L the latent heat of fusion and γ_{sl} the interface energy between solid and liquid. For smaller sizes, different approaches have been adopted [10,11].

[a] e-mail: carlo.bottani@polimi.it

Experimentally, it is well established [11,12] that

$$\frac{\Delta T}{T} = \frac{T_0 - T_{\rm M}}{T_0} \approx \frac{1}{R} \qquad (2)$$

which is simply the first order term in the series expansion of equation (1).

A thin liquid layer can exist even significantly below the melting temperature of the whole particle, which, as stated above, turns out to be considerably lower than the bulk melting temperature. In addition, the phase transition is characterized by an hysteresis cycle over a temperature range which could, in some cases, attain 150 K [3], which shows that melting takes place at temperatures above solidification (except for the very small sizes, where the hysteresis cycle disappears).

The size dependence of the melting temperature has been observed experimentally [11–15], using X-ray diffraction [16,19], transmission electron microscopy and optical reflectance [11,12,17].

In this paper we report the observation by Brillouin light scattering of an anomaly in the surface wave velocity in a thin amorphous SiO_x film containing Sn nanoparticles. This rapid drop in velocity over a small temperature range has already been tentatively attributed to the melting of the nanoparticles from the loss of Bragg peaks in parallel beam X-ray powder diffraction (XRD) measurements above and below the anomaly [21]. Here we show, studying 3 new samples, that the melting transition does indeed occur at the same temperature as the abrupt redshift in the Brillouin spectra and relate quantitatively the melting temperature to the measured size of the particles. Equation (1) has been verified. XRD provides also an evaluation of the strain content and thermal expansion of the particles.

2 Sample growth

The nanoparticles investigated in this work have been prepared by means of an evaporation-condensation technique in ultra-high vacuum (UHV) conditions [18]. On a substrate (silicon) kept at high temperature, a film of amorphous material (SiO_x) is evaporated. The material constituting the nanocrystals (Sn) is subsequently deposited on top in such a way that its vapour is condensed on the underlying dielectric layer. The amorphous nature of the dielectric layer and its non-wetting or partially wetting character with respect to the nanocrystals are essential characteristics of the technique. During evaporation, the temperature of the substrate is kept at such a value that nucleation of nanoparticles takes place in the liquid phase, so that the surface tension plays a dominant role in determining the shape of the nanodroplets, which is that of a truncated sphere. The liquid state of the deposit is an important step in the growth process, since it results in particles with a high degree of regularity. The temperature of the substrate is then lowered, so that the nanodroplets are frozen in the solid state, before being covered by an additional protecting amorphous layer; in this way, size and shape are kept constant. In order to improve the signal to noise ratio in the optical measurements, the total quantity of nanoparticles can be increased by replicating the above described depositions many times. The amorphous substrate was chosen to get a spatially isotropic distribution, a regular particle shape and a crystalline nature not induced by the matrix.

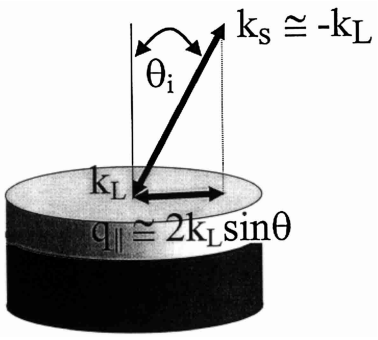

Fig. 1. Geometry of Brillouin scattering. $\theta_{\rm i}$ is the incidence angle, $k_{\rm L}$ is the incident phonon wavevector, $k_{\rm s}$ is the scattered wavevector and $q_\parallel$ is the phonon vector component parallel to the surface. The laser polarization is parallel to the surface. The scattered light is collected without polarization analysis.

If a small quantity of liquid material A is deposited on a substrate of a species B the intermolecular forces and the interfacial energies will lead to the optimisation of surface area in connection to the interfacial energy between A and B. Consequently, a particle of material A will not be able to take an arbitrary shape on the substrate B.

In our case the contact angle is $\varphi = 90°$ [20], so that ideally the particles have half-spherical shape. The size distribution is bimodal (presenting an interesting similarity with other systems) [18]; its larger portion ($\simeq 95\%$ in volume) is Gaussian-like and characterized by a relatively low size dispersion. The size range obtainable by changing growth parameters is quite wide, typically from ten to a few hundreds of nm. The parameter used to indicate the deposited nanoparticles material quantity in each layer is the so-called equivalent thickness, *i.e.* the thickness of the film containing the same volume of material, supposed to be continuous.

Three different SiO_x:Sn samples were deposited on similar Si substrates. Each contained the same volume amount of Sn but with different nanoparticle nominal radii: 2.5 nm (sample Sn1, equivalent thickness (e.t.) 1.25 nm); 10 nm (Sn2, e.t. 5 nm); 20 nm (Sn3, e.t. 10 nm). The overall thickness was 186 nm for all the samples. A blank sample of SiO_x, 186 nm thick, without Sn, was deposited for reference purposes.

3 Experimental setup

Surface Brillouin scattering data were recorded in a backscattering geometry at a fixed incidence angle ($\theta = 60°$), for all the samples and all the different temperatures, using a Sandercock six-pass tandem Fabry-Perot

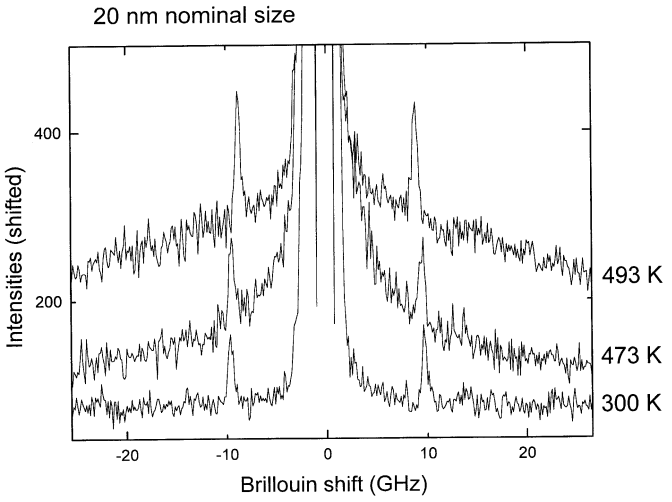

Fig. 2. Brillouin scattering for sample Sn3 at three different temperatures: room, before and after melting. Note the shift of the Rayleigh peak and the rising of a central feature.

interferometer (for the scattering geometry see Fig. 1). For the temperature control the samples were placed inside an Oxford Instruments cryothermostat Optistat DN-V with optical windows. The spectra were measured at different temperatures in the range 293−533 K, usually with a 10 K step and with a laser power of 40 mW incident onto the sample surface. This power was low enough not to enhance significantly the sample local temperature. Due to wave-vector conservation, surface phonons contributing to Brillouin scattering have a parallel wavelength $\lambda_{||} = \lambda_0/(2\sin\theta) \simeq 297$ nm, using the typical laser wavelength of an argon ion laser (514.5 nm). The acquisition time for each measurement was about 2 hours.

Parallel beam X-ray powder diffraction data were collected on the two circle diffractometer at station BM16 at the European Synchrotron Radiation Facility (ESRF) at Grenoble (France). The diffractometer consists of two high-precision, heavy-duty rotary tables aligned coaxially on a base plate; and a channel array of 111 oriented Ge crystals (single crystal analysers) each in front of a scintillation detector. Each channel is separated by 2° [22]. Two-dimensional images were captured by a CCD camera optically coupled to a phosphor screen.

A furnace for high-temperature powder diffraction measurements at temperatures up to 1600 °C was employed. However, there is a serious difficulty in producing an absolute calibration of the sample temperature due to the inability of locating a thermocouple directly on the (rotating) sample. As we were unable to determine the melting point directly from the furnace thermocouple, we had to perform an internal calibration [23] in which we determined the temperature directly from the measurement of the lattice parameter of the single crystal silicon substrate on which the SiO_x glass was deposited. (This method is widely applicable to high resolution powder diffraction, as silicon single crystal substrates are regularly used for their low background signal.)

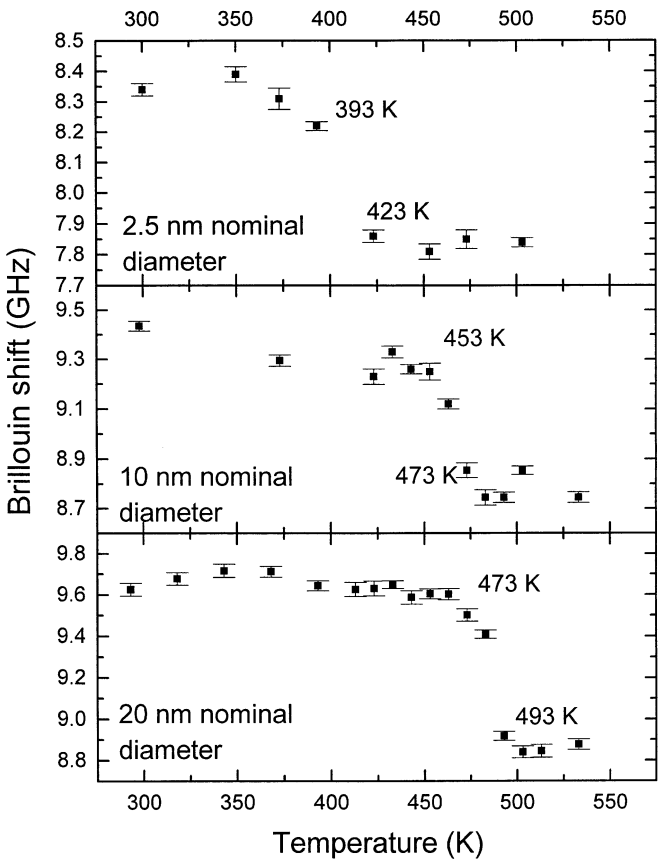

Fig. 3. Position of the Rayleigh peak as a function of temperature in sample Sn1 (top graph), Sn2 (middle) and Sn3 (bottom). Error bars are reported.

We monitored the Si 002 *forbidden* reflection and from the Si linear expansion coefficient, which is well documented [24–26], we were able to convert the nominal temperature read by the thermocouple into the true sample temperature.

The wavelength chosen was 0.055197 nm, and detector only scans were acquired, keeping the incident angle fixed at about 5°. The reason for using a small incidence angle is that this arrangement increases the X-ray path in the thin film, thus enhancing the interaction of the beam with the tin particles. The minimum value was limited by the geometry of the furnace.

4 Brillouin scattering

In Figure 2 Brillouin spectra from the sample Sn3 are shown. They correspond to three different temperatures (293 K room temperature, 473 K just below melting, 493 K just beyond melting). Two features are important: a Rayleigh peak whose shift is about 9 GHz, and a central peak whose intensity (and half width) was not constant with temperature.

In Figure 3 we show the experimental Rayleigh peak position as a function of temperature for the three samples. After an initially gradual variation the final shift

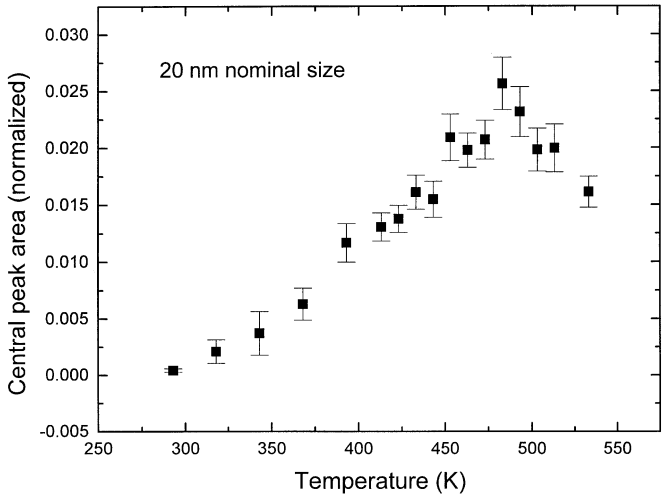

Fig. 4. Central peak area as a function of temperature in sample Sn3. Error bars are reported.

Table 1. Comparison between the melting temperature detected by XRD and the Rayleigh peak shift temperature, for the tin nanoparticles in samples Sn1, Sn2 and Sn3.

Sample	Brillouin Rayleigh peak shift (K)	XRD melting temperature (K)
Sn1	393−243	393−423
Sn2	453−473	443−463
Sn3	473−493	463−483

drop is rather sharp (it happens within a small temperature range, $\sim$ 20 K, but see the discussion below) and it is always of the order of 0.6 GHz. The transition temperature is $\sim$ 473−493 K for sample Sn3, $\sim$ 453−473 K for sample Sn2 and $\sim$ 393−423 K for sample Sn1 (Tab. 1).

The central feature, which is not present at room temperature, becomes more and more intense approaching the anomaly temperature. We show the behavior of the central peak area as a function of temperature for sample Sn3 in Figure 4.

5 X-Ray diffraction

The two-dimensional diffraction images recorded on the CCD camera showed continuous Sn diffraction rings corresponding to the β-tin reflections (Fig. 5) indicating that the nanoparticles were randomly oriented in the matrix, there being no preferred orientation with respect to the Si substrate. Equivalent images of the reference sample revealed no diffraction rings, confirming the amorphous nature of the silica matrix.

Figure 6 shows a section of the diffraction pattern recorded by the Ge analyser at room temperature for the sample Sn3. The four peaks detected (superimposed onto a varying background) index precisely to the 200, 101, 220, 211 diffraction peaks of the tetragonal structure of β-tin, which is the stable tin phase at room temperature (white tin). The first two peaks were individually resolved for samples Sn3 and Sn2, while only a broad band

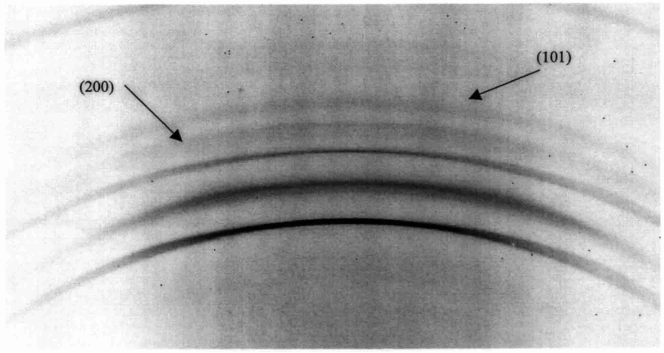

Fig. 5. CCD camera image of the diffraction rings in sample Sn3. The strong diffraction rings not labeled come from the sample holder.

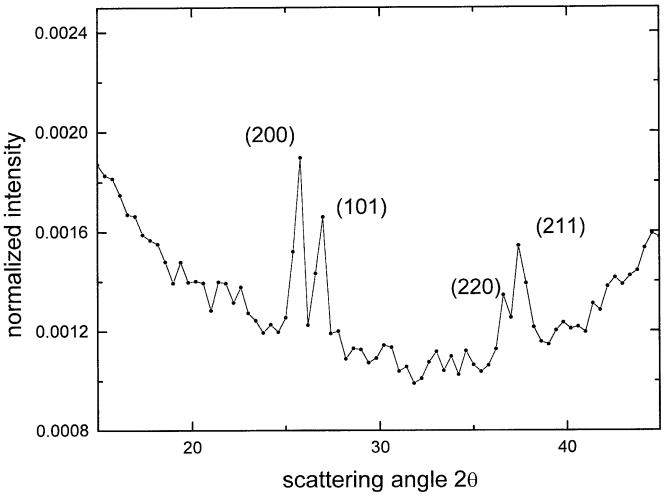

Fig. 6. Diffraction pattern from sample Sn3. In this measurement $\lambda = 0.13$ nm.

due to the superposition of two very broad and low intensity peaks could be detected for sample Sn1. We can thus affirm that at room temperature the nanoparticles are crystalline.

The peaks can be fitted well to Gaussian functions as well as to Pseudo-Voigt functions (combination of a Gaussian with a Lorentzian); a fit to Lorentzian functions is good, but not excellent in the case of sample Sn2. This could indicate the presence of a small amount of strain in this sample (see below for a discussion about the strain in sample Sn3). In Figure 7 Pseudo-Voigt fits to the peaks are shown (in sample Sn2 the weight of the Gaussian component is predominant with respect to that of the Lorentzian component). Using Scherrer's equation

$$L = \frac{0.94\lambda}{\Delta(2\theta)\cos\theta} \tag{3}$$

where λ is the X-ray wavelength, 2θ is the scattering angle and $\Delta(2\theta)$ is the FWHM (Full Width at Half Maximum) of the peak, we can determine the average particle size L. The FWHM value obtained from the fit is the same independently of the fitting function. The calculated values

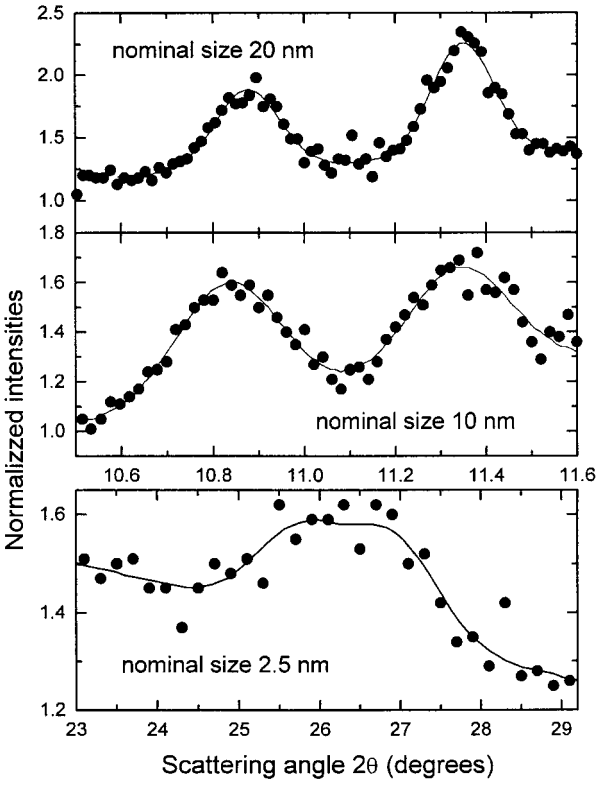

Fig. 7. (200) and (101) Bragg peaks of tin nanoparticles in sample Sn3 (top graph), Sn2 (middle) and Sn1 (bottom). Points represent experimental data, lines are Pseudo-Voigt fits to the two peaks. For sample Sn1, $\lambda = 0.13$ nm.

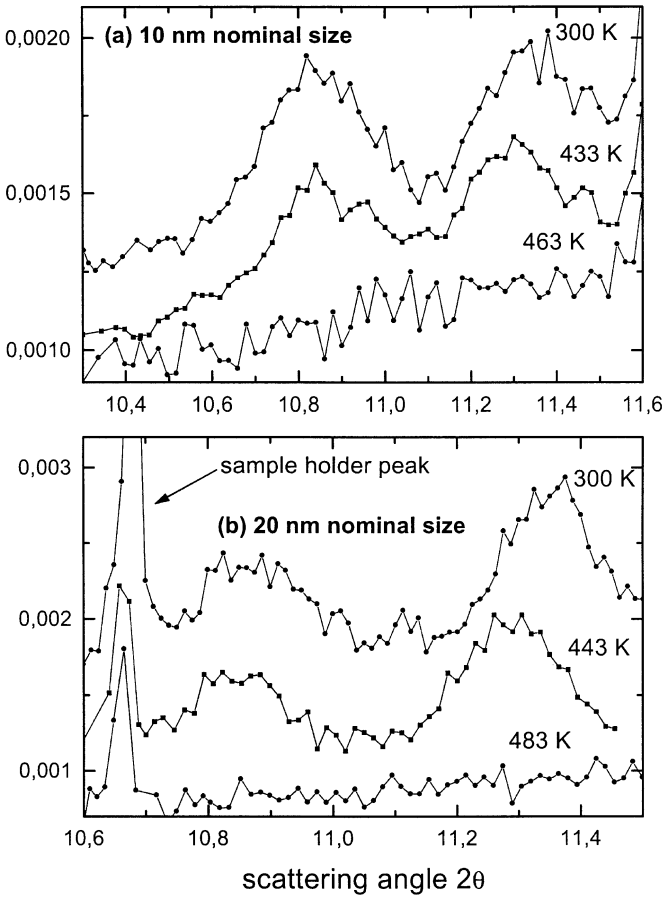

Fig. 8. (a) (200) and (101) tin peak evolution as a function of temperature in sample Sn2; (b) (200) and (101) tin peak evolution as a function of temperature in sample Sn3.

are 4.5 ± 2 nm (Sn1, nominal size 2.5 nm), 11 ± 1 nm (Sn2, nominal size 10 nm) and 18 ± 1 nm (Sn3, nominal size 20 nm). The agreement with the nominal values is good. As a function of temperature, the peaks change position systematically and the intensity falls to zero within a small temperature range (Fig. 8). The disappearance of the diffraction peaks indicates loss of crystalline order which we identify with the melting of the nanoparticles and occurs at the same temperature as the abrupt redshift in the Brillouin spectra. In Table 1 we compare the melting temperature determined for the three samples by Brillouin scattering and X-ray diffraction. Within the precision set by the temperature increments, the agreement is good. Figure 9 shows the melting temperature as a function of the particle size determined from the X-ray diffraction data. In all cases, the values are lower than the melting temperature of bulk tin, which is 505 K (232 °C). The solid line is a fit to equation (1), from which we determine the interfacial free energy between solid and liquid γ_{sl} to be $\simeq 0.1\ \mathrm{J\,m^{-2}}$. Even though equation (1) is strictly applicable only to spheres of radius greater than 15 nm [8,9] we believe that the γ_{sl} value we have evaluated is significant to an order of magnitude in our size range.

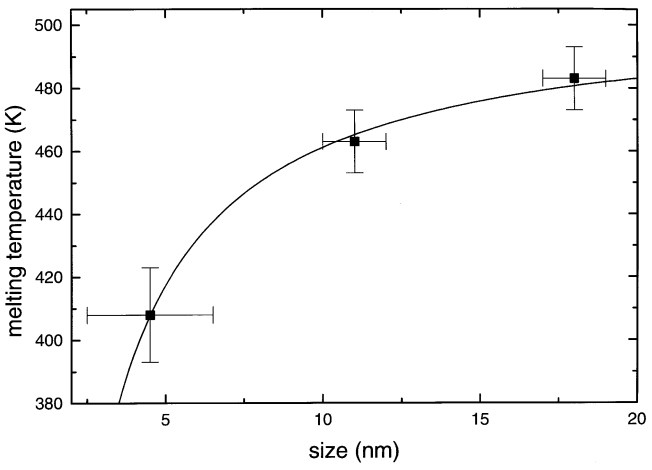

Fig. 9. Fit of equation (1) to experimental data. Error bars are reported.

After melting, cooling of the samples to room temperature did not result in the immediate recovery of the crystalline structure of the particles. We were unable

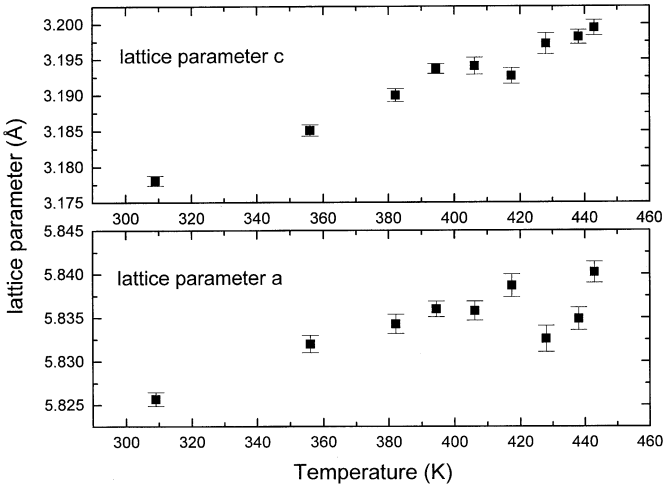

Fig. 10. Tin lattice parameters a and c as a function of temperature for sample Sn3. Error bars are reported.

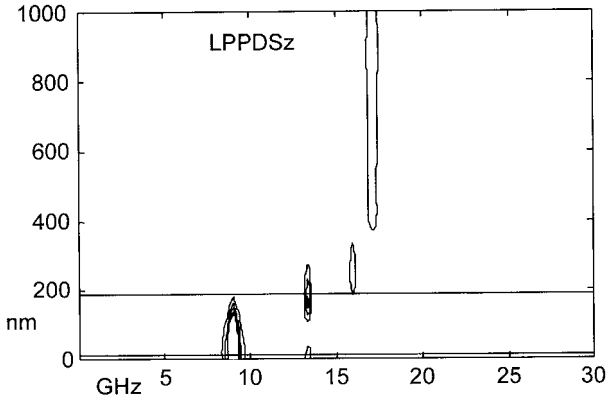

Fig. 11. Contour lines of the computed Layer Projected Phonon Density of States (LPPDS) as a function of the sample depth and frequency. The horizontal solid line at 186 nm represents the film-substrate interface.

to determine precisely the relaxation time, but it is in the region of one to two hours.

In the case of the larger nanoparticles (sample Sn3) the peaks were sufficiently sharp and intense to allow a precise determination of their position and as a consequence a precise estimate of the β-tin lattice parameters in the particles. The a and c values, determined from the (200) and (101) reflections, are plotted in Figure 10 in the temperature range 293−443 K. In the case of both samples Sn3 and Sn2, the measured values at room temperature are, within experimental errors, equal to the bulk values of $a = 0.583$ nm and $c = 0.318$ nm. This indicates that the nanoparticles are not subject to significant strain. The expansion, as temperature rises, is anisotropic. From Figure 10 we determine $\alpha_c \cong (50\pm10)\times10^{-16}$ K^{-1} for the expansion in the c direction and $\alpha_a \cong (20\pm5)\times10^{-16}$ K^{-1} for the a direction. This is consistent with the range of values for the anisotropic expansion reported in bulk single crystals ($\alpha_c = 30{-}40 \times 10^{-16}$ K^{-1} and $\alpha_a = 15{-}20\times10^{-16}$ K^{-1} over the range $300-500$ K [29]). The absence of any difference in expansion coefficients compared to the bulk values may again be taken as evidence of the absence of significant strain in the nanoparticles in sample Sn3.

The above conclusions are supported by a Hall analysis of strain [30–32,34]. Where finite size L and strain ε both contribute to the peak width we have

$$\frac{\Delta(2\theta)\cos\theta}{\lambda} = \frac{1}{L} + \varepsilon\frac{\sin\theta}{\lambda} \tag{4}$$

(if the size and distortion line profiles are presumed to be Lorentzian), or

$$\left(\frac{\Delta(2\theta)\cos\theta}{\lambda}\right)^2 = \left(\frac{1}{L}\right)^2 + \left(\varepsilon\frac{\sin\theta}{\lambda}\right)^2 \tag{5}$$

(if the profiles are presumed to be Gaussian). By determining with good precision the position and the FWHM of the first 4 diffraction peaks in sample Sn3, we conclude that the contribution of strain to the width of the peaks is very small and well below the detection limits ($\varepsilon \approx 1$) allowed by our data.

6 Discussion

The X-ray diffraction results show conclusively that the anomaly in the Brillouin spectra is a result of the melting of the nanoparticles. The surface Brillouin scattering measurements are consistent with this finding. The sample geometry was designed to have only one Brillouin active surface phonon travelling parallel to the surface and probing mainly the silica film containing the nanocrystals to obtain maximum sensitivity to changes of nanoparticle properties. In this way the suitable modified Rayleigh phonon is localized in the film and has only a vanishing tail in the silicon substrate. This result was achieved computing the layer projected phonon density of states and the corresponding Brillouin cross section using the software described in [27,28]. The results are shown in Figures 11 and 12 respectively. As the described computation requires the knowledge of the elastic constants of the film, the wavelength $\lambda_{||}$ of the Rayleigh phonon being much bigger than the particle radii, a rough estimate can be obtained treating the film as an effective medium with average elastic properties. In practice, the effective elastic constants B and μ (bulk and shear modulus, respectively) of a film with spherical inclusions were obtained within the Voigt-Reuss-Hill approximation [35] by the formulae

$$B = B_2 - f_1(B_2 - B_1)\frac{3B_2 + 4\mu_2}{3B_1 + 4\mu_2} \tag{6}$$

$$\mu = \mu_2 - f_1(\mu_2 - \mu_1)\frac{5\,(3B_2 + 4\mu_2)}{9B_2 + 8\mu_2 + 6(B_2 + 2\mu_2)\mu_1/\mu_2} \tag{7}$$

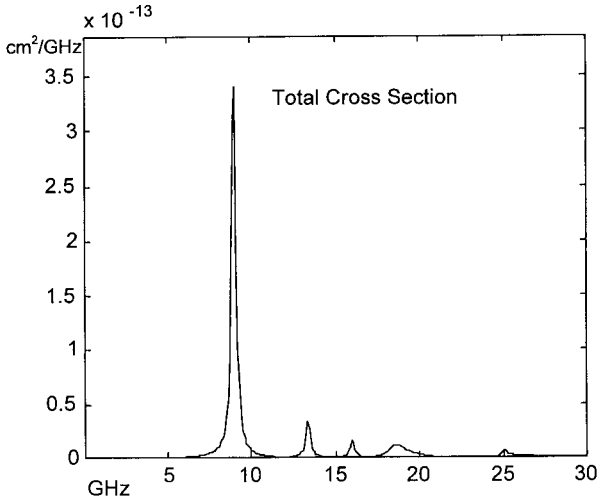

Fig. 12. Computed Brillouin cross-section for our samples, showing the expected Rayleigh peak at a frequency of about 9 GHz.

where we can neglect the elastic anisotropy of the tin nanocrystals (XRD shows that the tin crystals have random orientation with respect to the substrate). 1 is for tin and 2 for silica; f_1 is the tin volume fraction in the film. Figure 13 shows μ as a function of μ_1 for $f_1 = 0.2$, which is the fraction of tin in our samples.

In the case of very small size when the particles melt their shear modulus abruptly drops to a much lower value (liquid phase). The contribution of the variation of the Sn nanoparticle density to the effective medium density across melting is negligible. The effect of varying B_1 is negligible too, and if we roughly set $\mu_1 = 0$ in the liquid phase, the main effect of the melting is an abrupt lowering of μ. Melting of bigger particles instead is a two step process: first a surface melting and then a complete melting of the body of the particle. In real samples a size distribution exists leading to coexistence of solid, partially liquid and completely liquid particles at a given temperature. This corresponds to a progressive phase change in a rather wide temperature interval before the overall rather abrupt softening described above occurs. The softening of the shear modulus is responsible for the decrease of the Rayleigh wave velocity after melting.

In any case, the qualitative trend deducible from our crude model is in agreement with the experimental results and represents a good test for the interpretation reported above. A quantitative interpretation would require going beyond the effective medium approximation to take explicitly into account particle size effects and not only the Sn concentration.

The central peak area shows an increase when approaching the melting temperature. The central peak is wider than 30 GHz and so our data are not precise enough to study its behavior for all the samples or to investigate the width of the peak.

Its origin could possibly be related to the coupling of soft modes in the single particles with relaxing degrees of freedom through a damping process [33], arising from dynamic inhomogeneities in the semi-liquid particles in the vicinity of the phase transition. As the Rayleigh phonon is a mesoscopic excitation of the whole effective medium, it cannot be assumed as the soft mode characterizing the single particle melting. Since we are currently directly measuring such modes and their coupling with a central peak with a different technique, this aspect of the melting transition will be discussed elsewhere in the next future.

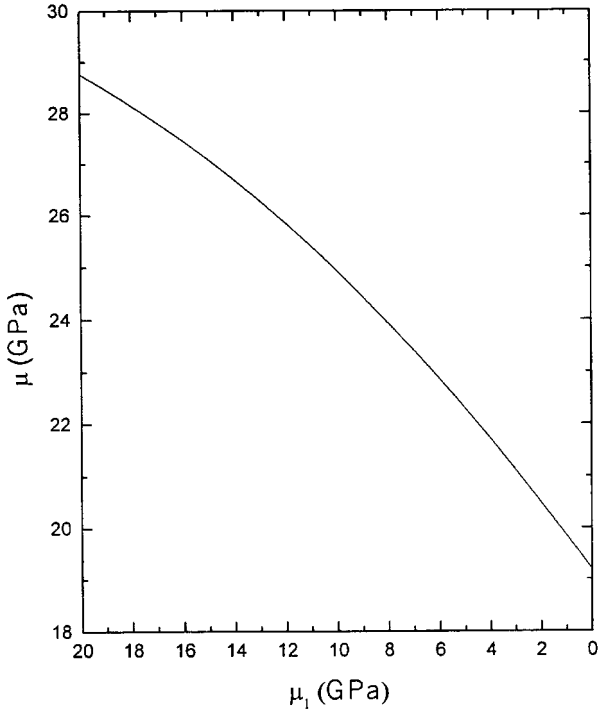

Fig. 13. Effective shear modulus μ of silica film containing a concentration $f_1 = 0.2$ of inclusions of shear modulus μ_1 *vs.* μ_1. For solid Sn nanocrystals $\mu_1 = 18$ GPa. For silica $\mu_2 = 31.2$ GPa and $B_2 = 36.9$ GPa. When Sn becomes liquid μ_1 drops to zero and μ reaches a minimum.

7 Conclusions

We have shown that the acoustic anomaly, observed in the Brillouin spectra of thin SiO_x thin films containing nanometre sized particles of Sn, arises from the melting of the particles, confirming the preliminary results reported in [21]. The melting transition observed in the X-ray diffraction measurements occurs in each case, within a 5 °C band, at the acoustic anomaly. Although the transition is quite wide, due to the significant spread in the particle size distribution, the melting temperature as a function of average particle size, which we have deduced from the X-ray diffraction data, agrees with current theoretical predictions, see equation (1). Within the limits of precision set by the intrinsically broad and weak diffraction peaks, the lattice parameters corresponded to those of unstrained bulk Sn crystals. The thermal expansion of the nanoparticles was anisotropic and the coefficients of thermal expansion in the a and c directions were found,

within the experimental error, to be the same as in bulk tin. This last observation also supports the contention that the particles are unstrained. The origin of the hysteresis in crystallisation is not fully understood and requires a more lengthy investigation, expensive on synchrotron radiation beamtime. As we have demonstrated elsewhere [27], the combination of elastic X-ray and inelastic light scattering from thin films enables key structural parameters to be obtained and used in the modelling of the Brillouin spectra. Once again we have demonstrated the ability of the effective medium approach to interpret subtle effects in Brillouin spectroscopy.

We would like to acknowledge help from Andy Fitch and Eric Dooryhee (BM16, ESRF) for X-ray diffraction measurements. A. Stella and P. Tognini acknowledge financial support from "Progetto finalizzato Materiali e Dispositivi per l'Elettronica dello Stato Solido" (MADESS II).

References

1. L. Banyai, S.W. Koch, *Semiconductor quantum dots* (World Scientific, Singapore, 1993).
2. U. Woggon, *Optical properties of semiconductor quantum dots* (Springer Verlag, Berlin, 1997).
3. A. Stella, P. Cheyssac, R. Kofman, *Science and Technology of Thin Films* (World Scientific, Singapore, 1996), p. 57.
4. U. Kreibig, M. Vollmer, *Optical Properties of Metal Clusters* (Springer, Berlin, 1995).
5. A. Stella, P. Tognini, P. Cheyssac, R. Kofman, Nuovo Cim. D **20**, 1249 (1998).
6. M. Nisoli, S. De Silvestri, A. Cavalleri, A.M. Malvezzi, A. Stella, G. Lanzani, P. Cheyssac, R. Kofman, Phys. Rev. B **55**, R13424 (1997).
7. N.T. Gladkikh, S.P. Chizhik, V.I. Larin, L.K. Grigor'eva, V.N. Sukhov, Izv. Acad. Nauk SSR Met. **5**, 196 (1982).
8. V.K. Semenchenko, *Surface phenomena in metals and alloys* (Pergamon Press, New York, 1981).
9. R. Kofman, P. Cheyssac, R. Garrigos, Y. Lereah, G. Deutscher, Z. Phys. D **20**, 267 (1991).
10. F. Ercolessi, W. Andreoni, E. Tosatti, Phys. Rev. Lett. **66**, 911 (1991).
11. R. Kofman, P. Cheyssac, A. Aouaj, Y. Lereah, G. Deutscher, T. Ben-David, J.M. Penisson, A. Bourret, Surf. Sci. **303**, 231 (1994).
12. A.N. Goldstein, C.M. Echer, A.P. Alivisatos, Science **256**, 1425 (1992).
13. Ph. Buffat, J.P. Borel, Phys. Rev. A **13**, 2287 (1976).
14. S.L. Lai, J.Y. Guo, V. Petrova, G. Ramanath, L.H. Allen, Phys. Rev. Lett. **77**, 99 (1996).
15. M. Schmidt, R. Kusche, B. von Issendorff, H. Haberland, Nature **393**, 238 (1998).
16. A. Di Cicco, Phys. Rev. Lett. **81**, 2942 (1998).
17. A. Stella, A. Migliori, P. Cheyssac, R. Kofman, Europhys. Lett. **26**, 265 (1994).
18. E. Sondergard, R. Kofman, P. Cheyssac. A. Stella, Surf. Sci. **364**, 467 (1996).
19. K.F. Peters, Yip-Wah Chung, J.B. Cohen, Appl. Phys. Lett. **71**, 2391 (1997).
20. E. Sondergard, R. Kofman, P. Cheyssac, F. Celestini, T. Ben-David, Y. Lereah, Surf. Sci. **388**, L1115 (1997).
21. C.E. Bottani, A. Li Bassi, B.K. Tanner, A. Stella, P. Tognini, P. Cheyssac, R. Kofman, Phys. Rev B **59**, R15601 (1999).
22. A.N. Fitch, Materials Science Forum **228**, 219 (1996); see also: `www.esfr.fr`.
23. A. Li Bassi, Ph.D. thesis, Durham University (2000).
24. A.K. Freund, J.A. Gillet, L. Zhang, *SPIE Conf. On Crystal and Multilayer Optics* (SPIE eds., San Diego, 1998), Vol. 3448.
25. K.G. Lyon, G.L. Salinger, C.A. Swenson, G.K. White, J. Appl. Phys. **48**, 865 (1977).
26. Y. Okada, Y. Tokumaru, J. Appl. Phys. **56**, 314 (1984).
27. M. Beghi, C.E. Bottani, P.M. Ossi, T. Lafford, B.K. Tanner, J. Appl. Phys. **81**, 672 (1997).
28. A. Amici, M.G. Beghi, C.E. Bottani, Comput. Mat. Sci. (to be published, 2000).
29. I.S. Grigoriev, E.Z. Meilikhov editors, *Handbook of Physical Quantities* (CRC Press, 1997).
30. S.B. Qadri, J.P. Yang, E.F. Skelton, B.R. Ratna, Appl. Phys. Lett. **70**, 1020 (1997).
31. W.H. Hall, Proc. Phys. Soc. London Sec. A **62**, 741 (1949).
32. G.K. Williamson, W.H. Hall, Acta Metall. **1**, 22 (1953).
33. V.L. Ginzburg, A.P. Levanyuk, A.A. Sobyanin, Phys. Rep. **57**, 151 (1980).
34. H.P. Klug, L.E. Alexander, *X-Ray Diffraction Procedures For Polycrystalline and Amorphous Materials* (John Wiley & Sons, New York, 1974).
35. G. Grimvall, *Thermophysical Properties of Materials*, (North-Holland, Amsterdam, 1986), p. 268.